Letter

Visualization of Surface-Acoustic-Wave Potential by Transmission-Mode Microwave Impedance Microscopy

Lu Zheng, Di Wu, Xiaoyu Wu, and Keji Lai*

Department of Physics, University of Texas at Austin, Austin, Texas 78712, USA

(Received 11 April 2018; published 20 June 2018; corrected 6 July 2018)

Elastic waves propagating in piezoelectric materials are accompanied by a time-varying electric potential, which is of critical importance for acoustoelectronic applications. The spatial mapping of such a potential at microwave frequencies is challenging since the characteristic length scale is determined by the acoustic wavelength of several micrometers. We report on the visualization of surface acoustic waves (SAWs) on ferroelectric samples by transmission-mode microwave impedance microscopy. The SAW potential launched by the interdigital transducer is detected by the tip and demodulated by the microwave electronics as time-independent spatial patterns. Wave phenomena such as interference and diffraction are imaged and the results are in excellent agreement with the theoretical analysis. Our work opens up an avenue to study various electromechanical systems in a spatially resolved manner.

DOI: 10.1103/PhysRevApplied.9.061002

The linear electromechanical coupling in piezoelectric materials enables the interconversion between electrical and acoustic signals [1], which has found numerous applications in modern science and technology [2,3]. For instance, the excitation and detection of surface acoustic waves (SAWs) in quartz crystals are widely utilized in electronic components such as delay lines, filters, and oscillators [2,3]. The oscillating potential carried by propagating SAWs can manipulate the two-dimensional electrons hosted in piezoelectric GaAs quantum wells [4,5]. In periodically poled superlattices of ferroelectric lithium niobate ($LiNbO_3$), the coupling between gigahertz (GHz) electromagnetic and acoustic waves leads to polaritons with different phononic band structures [6–11]. In these systems, the characteristic dimension is set by the acoustic wavelength in piezoelectric solids, which is 5 orders of magnitude smaller than the electromagnetic wavelength at the same frequency (f). Research work that provides spatial information in the mesoscopic length scale is therefore highly desirable for studying wave phenomena, such as the interference, diffraction, and localization, of few-gigahertz supersonic SAWs.

In the past few decades, much effort has been made to probe acoustoelectronic properties in a spatially resolved manner. Scanning laser interferometry, for example, images the out-of-plane displacement fields [12,13] with subpicometer sensitivity and a diffraction-limited lateral resolution around 1 μm. The spatial resolution of surface displacement fields can be improved to approximately 20 nm in scanning acoustic force microscopy, which detects the nonlinear mixing of two slightly detuned SAWs through a cantilever probe at the difference frequency [14–16]. The subnanometer SAW amplitude has also been visualized by stroboscopic x-ray imaging [17,18]. On the other hand, the piezoelectric SAW potential that is critical for the applications has not been thoroughly studied. It was demonstrated that the secondary electrons in a scanning electron microscope (SEM) could be modulated by the spatially varying SAW electric field [19,20]. The applicability of this method, however, is rather limited due to the strong charging effect in insulating piezoelectric crystals [19], resulting in a moderate resolution of about 1 μm and an operation frequency below 0.5 GHz. In this Letter, we report on the visualization of piezoelectric SAW potential on the surface of z-cut $LiNbO_3$ crystals by transmission-mode microwave impedance microscopy (TMIM), an atomic-force-microscopy (AFM)-based technique with sub-100-nm spatial resolution. The SAW potential generated by interdigital transducers (IDTs) is demodulated by the homodyne detection electronics, showing time-independent spatial patterns in the two orthogonal channels. The superposition of two counterpropagating SAWs and wave diffraction due to a small domain with opposite polarization are also observed by TMIM. Our work introduces an alternative direction to locally probe acoustoelectronic phenomena in complex systems by near-field electromagnetic imaging.

As a rapidly evolving technique in recent years, MIM is commonly used to study the nanoscale permittivity and conductivity distribution in advanced materials [21–24]. In a typical reflection-mode MIM (RMIM) setup shown in Fig. 1(a), the gigahertz signal is delivered to the probe through an impedance-match section [22]. The small variation of tip-sample impedance $Z_{t\text{-}s}$ during the

*kejilai@physics.utexas.edu

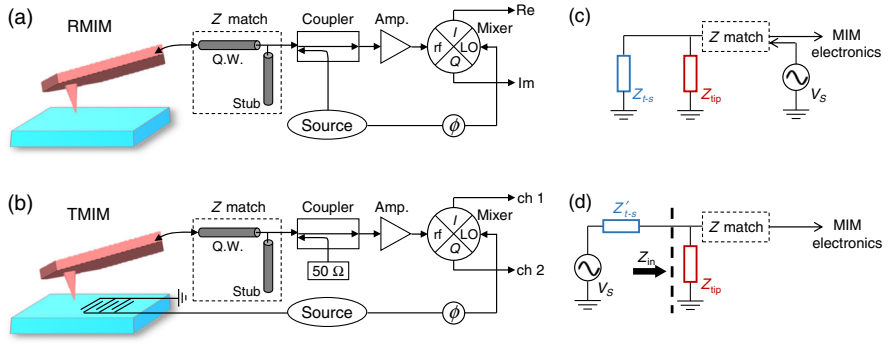

FIG. 1. (a) Schematic of RMIM. The excitation signal is delivered to the tip and the reflected signal is amplified and demodulated by the IQ mixer to form the RMIM-Re and -Im images. (b) Schematic of TMIM. The excitation signal is delivered to the IDT on the sample, and the transmitted signal is amplified and demodulated by the IQ mixer to form the TMIM–ch-1 and–ch-2 images. Equivalent circuits of (c) RMIM and (d) TMIM. Q.W. represents quarter-wave cable.

measurement leads to changes of the reflected microwave, which is demodulated by the in-phase quadrature (IQ) mixer. By adjusting the local oscillator (LO) phase ϕ, the real and imaginary components of the admittance change $\Delta Y_{t\text{-}s} = \Delta(Z_{t\text{-}s}{}^{-1})$ can be mapped as RMIM-Re or -Im images [22]. As shown in Fig. 1(b), it is straightforward to reconfigure the system as TMIM, where the tip acts as a receiver to detect the local rf voltage V_s. The equivalent circuits of RMIM and TMIM are schematically shown in Figs. 1(c) and 1(d), respectively. At our operation frequency of approximately 1 GHz, the cantilever probe [25] can be viewed as a lumped element dominated by an effective capacitance of 1 pF. Using transmission-line analysis [26] (Appendix A), it can be shown that the receiver has an input impedance $|Z_{\text{in}}| \sim 1$ kΩ at 1 GHz. Through a similar tip-sample coupling impedance $Z'_{t\text{-}s}$, an input signal of $V_{\text{in}} = V_s Z_{\text{in}}/(Z'_{t\text{-}s} + Z_{\text{in}})$ is picked up by the tip and then amplified and demodulated by the electronics. It is worth noting that similar transmission-type probes have been used to map out the rf fields in microwave resonators [27,28] and metamaterials [29,30]. In those systems, however, the characteristic length scale is determined by the electromagnetic wavelength (30 cm at 1 GHz), and a mesoscopic spatial resolution is not necessary.

Figure 2(a) shows the SEM image of a pair of IDTs used in our experiment. The device is designed to excite the x-propagating Rayleigh-type SAW on the z-cut $LiNbO_3$ substrate, which is poled to be a single ferroelectric domain prior to the device fabrication. $LiNbO_3$ has a trigonal crystal structure with a mirror y-z plane and a direct triad z axis along the polar direction [31]. Using finite-element modeling (Appendix B), one can show that the piezoelectric SAW potential V_s is about 10% of the excitation voltage at the transmitting IDT (±1 V). In addition, since the coupling impedance $Z'_{t\text{-}s}$ between the tip and the metal electrodes is much smaller than that between the tip and $LiNbO_3$, the signals on the IDTs are very strong and saturate the TMIM output. The S parameters of the two IDTs measured by a vector network analyzer are plotted in Fig. 2(b). The passband of about 50 MHz around 1 GHz is consistent with the use of 20 pairs of interdigitated fingers [2]. The dip of S_{12} in the middle of the passband is likely due to the SAW reflection from the receiving IDT.

Figure 2(c) displays the simultaneously acquired AFM and TMIM–channel-1 (ch 1) images when the excitation IDT is powered by a 10-dBm microwave at $f = 957$ MHz. While only the interdigitated fingers are seen in the surface topography, the electrical potential on both the IDT and the $LiNbO_3$ surface can be clearly imaged by TMIM. In Fig. 3, we focus on the data taken in an area of 10×20 μm between the two IDTs. The featureless RMIM images in Fig. 3(a) indicate that there is no permittivity or conductivity variation, whereas the two TMIM images in Fig. 3(b) exhibit sinusoidal patterns. As discussed before, the tip is picking up an input signal that is proportional to the SAW potential. Without loss of generality, the signals at the rf and LO ports of the mixer can be represented as $V_{\text{rf}} \propto V_s \propto e^{i(\omega t - kx)}$ and $V_{\text{LO}} \propto e^{i(\omega t + \phi)}$ (where ω is the angular frequency, k the acoustic wave vector, and ϕ the mixer phase), respectively. Ignoring the terms containing $2\omega t$, we obtain the output signals from the quadrature mixer as follows:

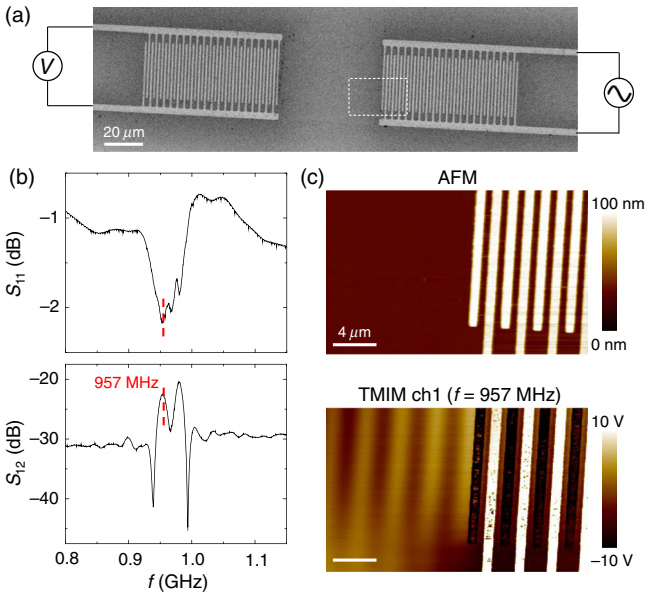

FIG. 2. (a) SEM image of the SAW device with a pair of IDTs. (b) Return loss S_{11} and insertion loss S_{12} of the SAW device measured by a vector network analyzer. The TMIM frequency of 957 MHz is labeled in the plots. (c) AFM and TMIM images in the dashed rectangular region in (a). Wavelike features are seen in the TMIM data. The scale bars are 4 μm.

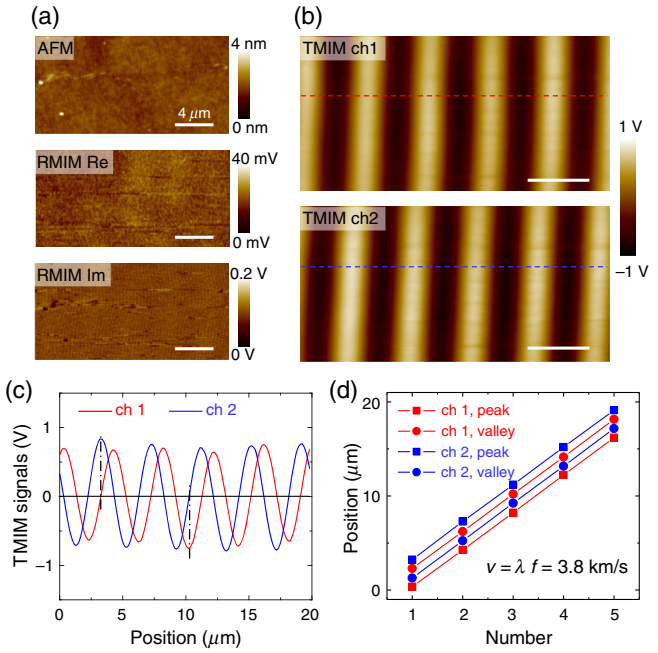

FIG. 3. (a) AFM and RMIM-Re and -Im images in an area between the two IDTs. (b) TMIM–ch-1 and–ch-2 images in the same area as (a). All scale bars are 4 μm. (c) Line profiles of the two TMIM channels. The dashed-dotted lines show that the two sinusoidal curves are offset by 90°. (d) Positions of the peaks and valleys in the TMIM data. The linear fits to the data points correspond to a Rayleigh SAW speed of 3.8 km/s.

$$V_{\mathrm{ch}\,1} \propto \mathrm{Re}(V_{\mathrm{rf}} V_{\mathrm{LO}}^{*}) = \cos(kx + \phi), \tag{1}$$

$$V_{\mathrm{ch}\,2} \propto \mathrm{Im}(V_{\mathrm{rf}} V_{\mathrm{LO}}^{*}) = -\sin(kx + \phi). \tag{2}$$

In other words, the electronics demodulate the time-varying SAW potential into time-independent spatial patterns, which is in good agreement with the TMIM data. The line profiles in Fig. 3(c) show the same amplitude and a phase difference of 90° between the two channels. We also confirm that a change in the mixer phase ϕ introduces the same phase shift to both channels. By fitting the periodicity of the sinusoidal curves, a phase velocity of $v = 3.8$ km/s is obtained, which is consistent with that of the x-propagating Rayleigh SAW [32]. Further analysis of the signal level (Appendix A) also shows that the tip-sample coupling impedance in our experiment $|Z'_{t\text{-}s}| \sim 160$ kΩ, which is much greater than $|Z_{\mathrm{in}}|$.

We now turn to the TMIM imaging of a standing wave formed by two counterpropagating SAWs. Figure 4(a) shows the schematic of the experimental setup, where two balanced signals (0 dBm in amplitude) with a phase offset of θ are fed into the pair of IDTs. This geometry is technologically important in that it can create acoustic trapping potentials for electrons [33]. Following the same analysis as above, the input signals to the mixer can be written as $V_{\mathrm{rf}} \propto e^{i(\omega t - kx)} + e^{i(\omega t + kx + \theta)}$ and $V_{\mathrm{LO}} \propto e^{i\omega t}$. The LO phase ϕ is omitted since it contributes the same phase to both channels. The mixer then generates two output signals, as follows:

$$V_{\mathrm{ch}\,1} \propto \mathrm{Re}(V_{\mathrm{rf}} V_{\mathrm{LO}}^{*}) = \cos kx + \cos(kx + \theta), \tag{3}$$

$$V_{\mathrm{ch}\,2} \propto \mathrm{Im}(V_{\mathrm{rf}} V_{\mathrm{LO}}^{*}) = -\sin kx + \sin(kx + \theta). \tag{4}$$

By tuning the phase difference θ between the two counterpropagating SAWs, the signal levels of the two TMIM channels can be varied. When $\theta = 0°$, the sinusoidal spatial patterns are expected to appear only in ch 1 ($V_{\mathrm{ch}\,1} \propto 2\cos kx$, $V_{\mathrm{ch}\,2} \propto 0$). The patterns should then be the same in both channels when $\theta = 90°$ ($V_{\mathrm{ch}\,1} = V_{\mathrm{ch}\,2} \propto \cos kx - \sin kx$) and completely move to ch 2 when $\theta = 180°$ ($V_{\mathrm{ch}\,1} \propto 0$, $V_{\mathrm{ch}\,2} \propto -2\sin kx$). As seen in Fig. 4(b), the predicted evolution is again in excellent agreement with the measured TMIM data. The results demonstrate that TMIM can probe the acoustic standing waves in piezoelectric materials.

Finally, we briefly discuss the visualization of SAW diffraction due to the presence of a small domain. $LiNbO_3$ wafers poled to be a single ferroelectric domain are energetically unstable. Over an extended period, small domains with opposite polarization may spontaneously form to reduce the electrostatic energy. The domain inversion flips the sign of odd-rank tensors (polarization, first rank; piezoelectric tensor, third rank), while leaving the even-rank tensors (permittivity, second rank; elasticity tensor, fourth rank) unchanged [31]. As the acoustic impedance is mostly dependent on the density and elasticity of the material, the SAW displacement field is not strongly affected by the domain structure. By contrast, the SAW electric field, which is the gradient of the SAW potential, changes sign across a domain wall due to the piezoelectric coupling. In our sample, a small domain with spontaneous polarization reversal is found near the left IDT [the AFM

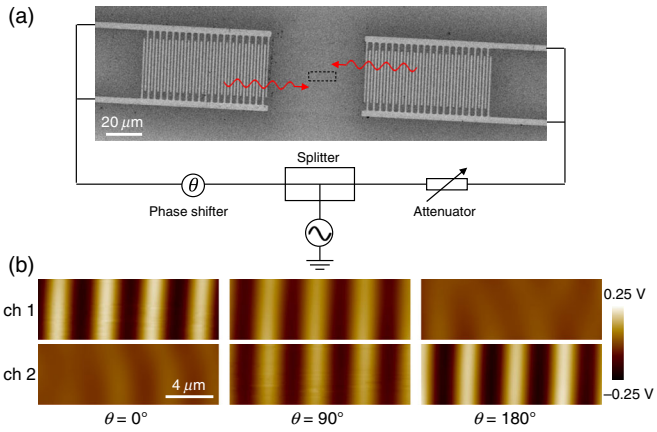

FIG. 4. (a) Schematic diagram for the imaging of counterpropagating waves. Two signals (0 dBm in amplitude and phase offset by θ) split from the same source are fed into the two IDTs. (b) TMIM images at different values of θ showing the transition of signal strength from ch 1 to ch 2.

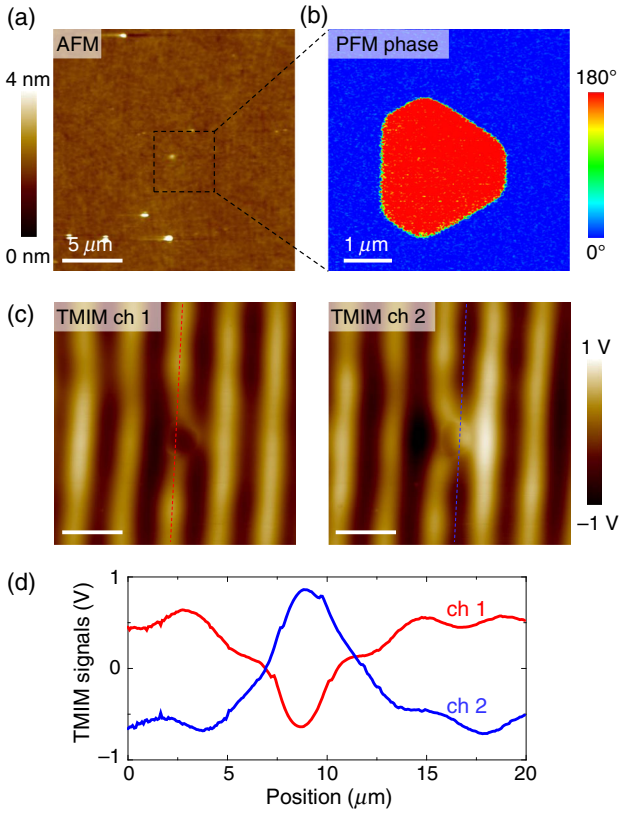

FIG. 5. (a) AFM image in an area with a spontaneously reversed domain. (b) Close-up view of the PFM phase image inside the dashed square of (a). The polarization reversal of the internal domain is evident from the 180° phase contrast. (c) TMIM–ch-1 and–ch-2 images in the same area as (a). Strong distortion of the wave front is seen around the small domain. The scale bars are 5 μm. (d) TMIM line profiles in (c) showing the sign change of the piezoelectric potential in the opposite domain.

image in Fig. 5(a)], as seen in the piezoresponse force microscopy (PFM) image in Fig. 5(b). Since its dimension is comparable to the acoustic wavelength, wave diffraction is expected around the domain. In Fig. 5(c), the TMIM surface potential maps indeed display very strong distortion of the wave front in this region. The line profiles in Fig. 5(d) further verify that the TMIM signals from both channels switch sign when passing through the small domain. The capability to resolve the spatial distribution of SAW potential is of particular interest to phononic metamaterials based on periodic ferroelectric domain structures [6–11].

To summarize, we demonstrate the visualization of piezoelectric SAW potential on z-cut $LiNbO_3$ surface by transmission-mode microwave imaging. The traveling or standing SAW potential generated by IDTs is demodulated by the microwave electronics and mapped as stationary spatial patterns. The signals can be explained by the standard microwave analysis. The wave diffraction due to a spontaneously reversed domain is also seen in the TMIM images. Our work paves the way to probe nanoscale acoustoelectronic behaviors in SAW devices, quantum materials, and phononic crystals.

ACKNOWLEDGMENTS.—This research was supported by NSF Division of Materials Research Grant No. DMR-1707372. The authors thank H. Dong, D. Sounas, and A. Alu for the helpful discussions.

APPENDIX A: MICROWAVE CIRCUIT ANALYSIS.—The quantitative analysis of the TMIM circuit is provided here. The cantilever probe [25] can be modeled as a lumped RLC element with $R_{tip} = 4\,\Omega$, $L_{tip} = 2$ nH, and $C_{tip} = 1$ pF. At $f = 1$ GHz, the effective tip impedance $|Z_{tip}| \sim 150\,\Omega$ is dominated by the capacitive reactance. As shown in Fig. 6(a), an impedance-match network consisting of a quarter-wave cable (Astrolab, Astro-Boa-Flex III, about 5 cm) and a tuning stub (Micro-Coax, UT-085C-TP, approximately 5 cm) is needed to route the tip impedance to the 50-Ω transmission line [22]. Figure 6(b) shows the calculated return loss Γ of the Z-match circuit, which agrees with the result measured by a vector network analyzer. Using

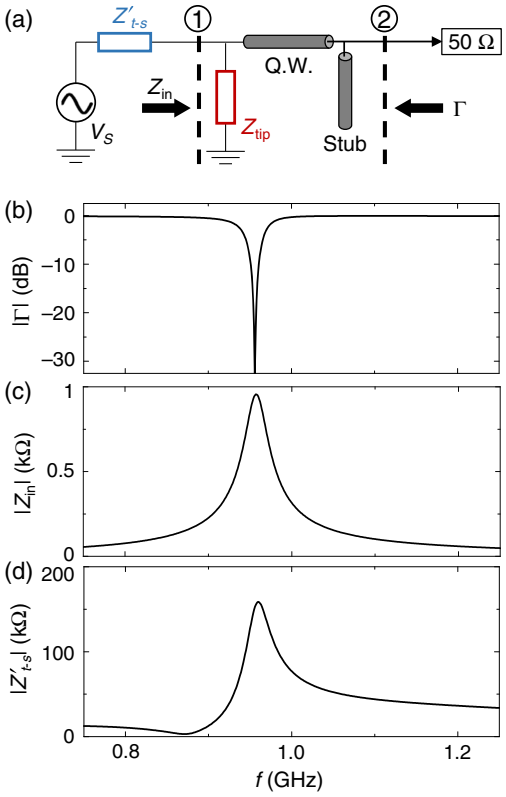

FIG. 6. (a) Equivalent circuit of the TMIM tip and the Z-match network. (b)–(d) Simulated return loss of the Z-match circuit, input impedance of the tip as a receiver, and tip-sample coupling impedance. The matching frequency with a minimal value of $|\Gamma|$ is used as the operation frequency for both the RMIM and TMIM modes.

the standard transmission-line analysis [26], one can then compute the effective impedance viewed from the tip side, i.e., the input impedance $Z_{\rm in}$ of the receiver. For the TMIM experiment, a large $|Z_{\rm in}|$ value is desirable for signal pickup. As shown in Fig. 6(c), $|Z_{\rm in}|$ reaches a maximum of about 1 kΩ at the matching frequency, which is used as the operation frequency for both RMIM and TMIM.

The tip-sample coupling impedance $Z'_{t\text{-}s}$ is estimated as follows. First, the relation between V_1 and V_2 [Fig. 6(a)] can be analyzed by considering the forward and backward propagating waves in the quarter-wave cable. On the other hand, these two voltages provide the link between the source signal V_s and the MIM output signal $V_{\rm MIM\,out}$:

$$V_1 = V_s Z_{\rm in}/(Z_{\rm in} + Z'_{t\text{-}s}) \approx V_s Z_{\rm in}/Z'_{t\text{-}s}, \qquad \text{(A1)}$$

$$V_2 = V_{\rm MIM\,out}/G_{\rm MIM}. \qquad \text{(A2)}$$

Here, $G_{\rm MIM} = 86$ dB is calibrated for the TMIM electronics. Based on our experimental data, a peak-to-peak SAW potential of 0.2 V (Appendix B) corresponds to a peak-to-peak TMIM output signal of approximately 2 V [Fig. 3(c)]. The computed tip-sample coupling impedance is plotted in Fig. 6(d). The result shows that, in this particular experiment, $|Z'_{t\text{-}s}|$ is around 160 kΩ, or an effective capacitance of 1 fF, at 1 GHz. Note that $Z'_{t\text{-}s}$ strongly depends on the tip-apex condition and the sample properties. A small value of $Z'_{t\text{-}s}$ is desirable for efficient TMIM detection, which, however, usually comes at the price of a blunt tip and reduced spatial resolution.

APPENDIX B: FINITE-ELEMENT MODELING.— The piezoelectric SAW potential can be numerically computed by the Structural Mechanics Module in commercial finite-element analysis software COMSOL 4.4. Here, we simulate a thin plate (1 μm in thickness) with a periodic boundary condition along the y direction. The $LiNbO_3$ region, whose permittivity, piezoelectric coefficient, and elasticity tensor are taken from Ref. [31], is bounded by the perfectly matched layer to avoid wave reflection from the boundary. The IDT spacing is set to be 3.8 μm. Alternating voltage (1 V in amplitude and 1 GHz in frequency) and ground (0 V) are applied on the IDT fingers to excite the x-propagating Rayleigh-type SAW on the z-cut $LiNbO_3$ surface. Figure 7(a) shows the simulated piezoelectric potential distribution in the sample, where the SAW is clearly seen. The surface potential from the simulation [Fig. 7(b)] indicates that the peak-to-peak SAW potential is 0.2 V, which is the source signal for the TMIM measurement. Using this information in Eq. (A1), we are able to evaluate the tip-sample coupling impedance $Z'_{t\text{-}s}$, which is crucial to understanding the signal level in our TMIM experiment in a quantitative manner.

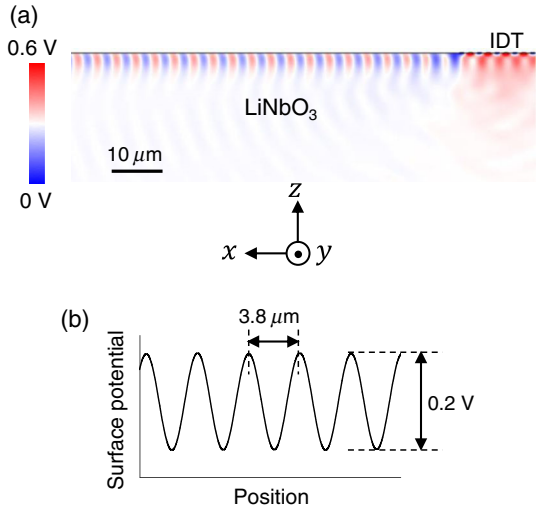

FIG. 7. (a) Piezoelectric potential distribution simulated by finite-element modeling. The voltage on the IDT fingers in this snapshot is 1 V/0 V. (b) Simulated SAW potential as a function of the position.

[1] D. Royer and E. Dieulesaint, *Elastic Waves in Solids* (Springer-Verlag Berlin, 1999).
[2] K.-y. Hashimoto, *Surface Acoustic Wave Devices in Telecommunications—Modeling and Simulation* (Springer-Verlag, Berlin, 2000).
[3] R. Weigel, D. P. Morgan, J. M. Owens, A. Ballato, K. M. Lakin, K.-y. Hashimoto, and C. C. W. Ruppel, Microwave acoustic materials, devices, and applications, IEEE Trans. Microwave Theory Tech. **50**, 738 (2002).
[4] S. Hermelin, S. Takada, M. Yamamoto, S. Tarucha, A. D. Wieck, L. Saminadayar, C. Bauerle, and T. Meunier, Electrons surfing on a sound wave as a platform for quantum optics with flying electrons, Nature (London) **477**, 435 (2011).
[5] R. P. G. McNeil, M. Kataoka, C. J. B. Ford, C. H. W. Barnes, D. Anderson, G. A. C. Jones, I. Farrer, and D. A. Ritchie, On-demand single-electron transfer between distant quantum dots, Nature (London) **477**, 439 (2011).
[6] Y.-Q. Lu, Y.-Y. Zhu, Y.-F. Chen, S.-N. Zhu, N.-B. Ming, and Y.-J. Feng, Optical properties of an ionic-type phononic crystal, Science **284**, 1822 (1999).
[7] Y.-y. Zhu, X.-j. Zhang, Y.-q. Lu, Y.-f. Chen, S.-n. Zhu, and N.-b. Ming, New Type of Polariton in a Piezoelectric Superlattice, Phys. Rev. Lett. **90**, 053903 (2003).
[8] C.-p. Huang and Y.-y. Zhu, Piezoelectric-Induced Polariton Coupling in a Superlattice, Phys. Rev. Lett. **94**, 117401 (2005).
[9] R.-C. Yin, C. He, M.-H. Lu, Y.-Q. Lu, and Y.-F. Chen, Polaritons in an artificial ionic-type crystal made of two-dimensional periodically inversed multi-domain ferroelectric crystals, J. Appl. Phys. **109**, 064110 (2011).
[10] D. Yudistira, A. Boes, D. Janner, V. Pruneri, J. Friend, and A. Mitchell, Polariton-based band gap and generation of surface acoustic waves in acoustic superlattice lithium niobate, J. Appl. Phys. **114**, 054904 (2013).

[11] D. Yudistira, A. Boes, B. Djafari-Rouhani, Y. Pennec, L. Y. Yeo, A. Mitchell, and J. R. Friend, Monolithic Phononic Crystals with a Surface Acoustic Band Gap from Surface Phonon-Polariton Coupling, Phys. Rev. Lett. **113**, 215503 (2014).

[12] Y. Sugawara, O. B. Wright, O. Matsuda, M. Takigahira, Y. Tanaka, S. Tamura, and V. E. Gusev, Watching Ripples on Crystals, Phys. Rev. Lett. **88**, 185504 (2002).

[13] D. M. Profunser, O. B. Wright, and O. Matsuda, Imaging Ripples on Phononic Crystals Reveals Acoustic Band Structure and Bloch Harmonics, Phys. Rev. Lett. **97**, 055502 (2006).

[14] T. Hesjedal and G. Behme, High-resolution imaging of a single circular surface acoustic wave source: Effects of crystal anisotropy, Appl. Phys. Lett. **79**, 1054 (2001).

[15] T. Hesjedal, Surface acoustic wave-assisted scanning probe microscopy—A summary, Rep. Prog. Phys. **73**, 016102 (2010).

[16] I. Yahyaie, D. A. Buchanan, G. E. Bridges, D. J. Thomson, and D. R. Oliver, High-resolution imaging of gigahertz polarization response arising from the interference of reflected surface acoustic waves, IEEE Trans. Ultrason. Ferroelectr. Freq. Control **59**, 1212 (2012).

[17] E. Zolotoyabko, D. Shilo, W. Sauer, E. Pernot, and J. Baruchel, Visualization of 10 μm surface acoustic waves by stroboscopic x-ray topography, Appl. Phys. Lett. **73**, 2278 (1998).

[18] W. Sauer, M. Streibl, T. H. Metzger, A. G. C. Haubrich, S. Manus, A. Wixforth, J. Peisl, A. Mazuelas, J. Härtwig, and J. Baruchel, X-ray imaging and diffraction from surface phonons on GaAs, Appl. Phys. Lett. **75**, 1709 (1999).

[19] D. V. Roshchupkin, Th. Fournier, M. Brunel, O. A. Plotitsyna, and N. G. Sorokin, Scanning electron microscopy observation of excitation of the surface acoustic waves by the regular domain structures in the $LiNbO_3$ crystals, Appl. Phys. Lett. **60**, 2330 (1992).

[20] D. V. Roshchupkin, M. Brunel, R. Tucoulou, E. Bigler, and N. G. Sorokin, Reflection of surface acoustic waves on domain walls in a $LiNbO_3$ crystal, Appl. Phys. Lett. **64**, 164 (1994).

[21] K. Lai, W. Kundhikanjana, M. Kelly, and Z. X. Shen, Nanoscale microwave microscopy using shielded cantilever probes, Appl. Nanosci. **1**, 13 (2011).

[22] K. Lai, W. Kundhikanjana, M. Kelly, and Z. X. Shen, Modeling and characterization of a cantilever-based near-field scanning microwave impedance microscope, Rev. Sci. Instrum. **79**, 063703 (2008).

[23] K. Lai, M. Nakamura, W. Kundhikanjana, M. Kawasaki, Y. Tokura, M. A. Kelly, and Z.-X. Shen, Science **329**, 190 (2010).

[24] D. Wu, A. J. Pak, Y. Liu, Y. Zhou, X. Wu, Y. Zhu, M. Lin, Y. Han, Y. Ren, H. Peng, Y.-H. Tsai, G. S. Hwang, and K. Lai, Thickness-dependent dielectric constant of few-layer In_2Se_3 nanoflakes, Nano Lett. **15**, 8136 (2015).

[25] Y. L. Yang, K. Lai, Q. Tang,W. Kundhikanjana, M. A. Kelly, K. Zhang, Z.-X. Shen, and X. Li, Batch-fabricated cantilever probes with electrical shielding for nanoscale dielectric and conductivity imaging, J. Micromech. Microeng. **22**, 115040 (2012).

[26] D. M. Pozar, *Microwave Engineering* (John Wiley & Sons, New York, 2012).

[27] A. S. Thanawalla, S. K. Dutta, C. P. Vlahacos, D. E. Steinhauer, B. J. Feenstra, Steven M. Anlage, F. C. Wellstood, and R. B. Hammond, Microwave near-field imaging of electric fields in a superconducting microstrip resonator, Appl. Phys. Lett. **73**, 2491 (1998).

[28] S. K. Dutta, C. P. Vlahacos, D. E. Steinhauer, Ashfaq S. Thanawalla, B. J. Feenstra, F. C. Wellstood, S. M. Anlage, and H. S. Newman, Imaging microwave electric fields using a near-field scanning microwave microscope, Appl. Phys. Lett. **74**, 156 (1999).

[29] K. Lai, T. Ma, X. Bo, S. Anlage, and G. Shvets, Experimental realization of a reflections-free compact delay line based on a photonic topological insulator, Sci. Rep. **6**, 28453 (2016).

[30] F. Gao, H. Xue, Z. Yang, K. Lai, Y. Yu, X. Lin, Y. Chong, G. Shvets, and B. Zhang, Topologically protected refraction of robust kink states in valley photonic crystals, Nat. Phys. **14**, 140 (2018).

[31] R. S. Weis and T. K. Gaylord, Lithium niobate: Summary of physical properties and crystal structure, Appl. Phys. A **37**, 191 (1985).

[32] K. Yamanouchi and K. Shibayama, Propagation and amplification of Rayleigh waves and piezoelectric leaky surface waves in $LiNbO_3$, J. Appl. Phys. **43**, 856 (1972).

[33] M. J. A. Schuetz, J. Knörzer, G. Giedke, L. M. K. Vandersypen, M. D. Lukin, and J. I. Cirac, Acoustic Traps and Lattices for Electrons in Semiconductors, Phys. Rev. X **7**, 041019 (2017).

Correction: Section headings at the end of the paper were misset and have been corrected.